NASA Reference Publication 1056

Orbiter Landing Loads Math Model Description and Correlation With ALT Flight Data

David A. Hamilton, John A. Schliesing,
and George A. Zupp, Jr.

JANUARY 1980

NASA

ERRATA

NASA Reference Publication 1056

ORBITER LANDING LOADS MATH MODEL DESCRIPTION AND CORRELATION WITH ALT FLIGHT DATA

David A. Hamilton, John A. Schliesing, and George A. Zupp, Jr.
January 1980

Page 3, second column, lines 28 and 29: The symbol "V_{head_i}" should be changed to "V_{total_i}" and the definition should read "volume of ith strut when fully extended, m^3 (in^3)"

Page 8: Equation (9) should be

$$F_{\text{damp}_i} = C_{\text{damp}_i} \dot{\delta}_{S_i}^2 \frac{\dot{\delta}_{S_i}}{\left|\dot{\delta}_{S_i}\right|}$$

Page 8: Equation (10) should be

$$F_{\text{air}_i} = P_{o_i} A_{\text{piston}_i}^{1-K_i} \left[\frac{V_{\text{total}_i}}{\frac{V_{\text{total}_i}}{A_{\text{piston}_i}} - \delta_{S_i}} \right]^{K_i}$$

Page 8, second column, lines 31 and 32: The symbol "V_{head_i}" should be changed to "V_{total_i}" and the definition should read "V_{total_i} is the volume of the strut when fully extended."

Issued 3-14-80

NASA Reference Publication 1056

Orbiter Landing Loads Math Model Description and Correlation With ALT Flight Data

David A. Hamilton, John A. Schliesing,
and George A. Zupp, Jr.
Lyndon B. Johnson Space Center
Houston, Texas

National Aeronautics
and Space Administration

**Scientific and Technical
Information Office**

1980

CONTENTS

TABLES

FIGURES

Orbiter Landing Loads Math Model Description and Correlation With ALT Flight Data

David A. Hamilton, John A. Schliesing, and George A. Zupp, Jr.

SUMMARY

In recent years, there has been a trend to use rational analysis in defining the touchdown dynamics of aircraft. This trend has precipitated efforts to correlate these analyses with measured landing dynamic data. Along this line, a mathematical model of the Space Shuttle Orbiter landing dynamics was developed and verified using measured landing loads data from the Shuttle Approach and Landing Test (ALT) Program. The correlation between analysis and test demonstrates the ability to accurately predict landing dynamics and the resulting landing loads on a flight vehicle. The key elements in the accuracy of correlation in the mathematical model are the landing gear strut stroking, fore-and-aft and lateral strut bending, and tire "spin-up" characteristics. Also modeled are the aerodynamic forces and moments on the Orbiter, including control surface effects.

Detailed correlations in the time domain between analysis and test of the landing gear "spin-up" and "spring-back" loads are presented, with peak loads agreeing well in both magnitude and frequency. Other landing gear parameters such as strut stroke and wheel rotational velocity are also correlated. Conclusions from these studies are included.

INTRODUCTION

The advent of the Space Shuttle Program has added a new dimension to the concept of reusable spacecraft. The Space Shuttle launch vehicle is composed of four principal structural elements: two solid rocket boosters, an Orbiter, and an external tank that provides liquid hydrogen and oxygen to the Orbiter main engines. The solid rocket boosters and the Orbiter are reusable. The primary sequencing points in the Shuttle trajectory are (1) lift-off, (2) solid rocket booster staging at approximately 120 seconds into the mission, and (3) end-burn and external tank staging at approximately 500 seconds into the mission. At this point, the Orbiter continues on into Earth orbit carrying payloads of as much as 29 500 kilograms (65 000 pounds). Once the payloads have been deployed, recovered, etc., and the orbital activity has been concluded, the Orbiter will enter the Earth's atmosphere and land.

The Orbiter is a delta-wing spacecraft designed to enter the atmosphere at orbital speeds and maneuver to a designated landing site. The Orbiter lands unpowered on a conventional runway. The landing system is a typical tricycle configuration with a nose gear and two main gears. The landing system is designed to handle approach speeds above 100 m/s (200 knots) with a sink speed of as much as 2.9 m/s (9.6 ft/s).

The magnitude of the initial landing loads dictates the size of a significant portion of the Orbiter structures; therefore, precise knowledge of the landing loads can result in a significant structural weight saving. In an effort to minimize the Orbiter structural weight, a detailed mathematical model of the Orbiter touchdown dynamics was developed and programed on a digital computer.

In the detailed simulation of the Orbiter touchdown dynamics, the Space Shuttle Orbiter is idealized as a pseudorigid structure to which a landing gear system is attached. The landing gear system is made of telescoping oleo-pneumatic struts and pneumatic tires. The aerodynamic forces acting on the Orbiter during landing are approximated by "six-degree-of-freedom" nonlinear aerodynamic equations with aerodynamic control coming from the deflection of the Orbiter's rudder, body flaps, elevons, and ailerons.

This report includes a definition of the pertinent coordinate systems and coordinate transformations. The equations of motion governing both a rigid vehicle and landing gear dynamics are presented. Con-

siderable detail is provided in defining the kinematic relationships used to model the articulating landing gear geometry.

The purpose of this report is twofold: (1) to document the analytical procedures used in developing a mathematical model of the Space Shuttle Orbiter touchdown dynamics and the quality of comparisons between the predicted results and the flight data, and (2) to make these procedures available to others who may be confronted with the task of mathematically modeling the touchdown dynamics of an oleo-pneumatic-type landing gear system.

In compliance with NASA's publication policy, the original units of measure have been converted to the equivalent value in the Système International d'Unités (SI). As an aid to the reader, the SI units are written first and the original units are written parenthetically thereafter.

SYMBOLS

A_{piston_i}	piston area of ith strut, cm^2 (in^2)
C_{Bx_i}	fore-and-aft damping coefficient of ith gear strut, N-s/m (lb-s/ft)
C_{By_i}	lateral damping coefficient of ith gear strut, N-s/m (lb-s/ft)
C_{damp_i}	damping coefficient of ith strut (nonlinear), N-s^2/m^2 (lb-s^2/ft^2)
$[C]_j$	matrix of jth measurement calibration constants
D_{A1_i}, D_{B1_i}	trunnion drag forces on ith gear, N (lb)
EI_{x_i}	average fore-and-aft bending stiffness of ith strut, N-cm^2 (lb-in^2)
EI_{y_i}	average lateral bending stiffness of ith strut, N-cm^2 (lb-in^2)
$\overrightarrow{F}_A$	aerodynamic force vector at reference point, N (lb)
$\overrightarrow{F}_{A_{\text{c.g.}}}$	aerodynamic force vector at c.g., N (lb)
F_{air_i}	force from compression of air spring of ith strut, N (lb)
F_{B1_i}	lower bearing force on ith gear, N (lb)
F_{B2_i}	upper bearing force on ith gear, N (lb)
F_{Br_i}	bearing friction force from stroking of ith strut, N (lb)
F_{Bx_i}	bending force of ith strut in X_B direction, N (lb)
F_{By_i}	bending force of ith strut in Y_B direction, N (lb)
F_{bend_i}	bending force in ith strut, N (lb)
F_{D_i}	drag force on ith gear perpendicular to strut axis and in X_B-Z_B plane, N (lb)
F_{damp_i}	damping force in ith strut, N (lb)
F_{strut_i}	total strut force acting in stroking direction of ith strut, N (lb)
F_{v_i}	vertical ground reaction force of ith gear, N (lb)
FX_A, FY_A, FZ_A	aerodynamic force vector components in the body coordinate system, N (lb)
F_{ϕ_i}	side force on ith gear perpendicular to strut axis and in the Y_B direction, N (lb)
I_{p_i}	polar moment of inertia of ith wheel, kg-m^2 (slug-ft^2)
I_{xx}, I_{yy}, I_{zz}	mass moments of inertia of the Orbiter, kg-m^2 (slug-ft^2)
I_{xz}, I_{yz}, I_{zz}	mass products of inertia of the Orbiter, kg-m^2 (slug-ft^2)
K_{b_i}	axial stiffness of ith gear drag brace, N/m (lb/ft)

K_i	gas constant for ith strut
K_{RT_i}	damping coefficient of ith tire, N-s/m (lb-s/ft)
K_{tire_i}	spring rate of ith tire, N/m (lb/ft)
L_{b_i}	length between ith gear bearing points when gear is fully extended, m (ft)
L_i	strut length from axle to upper bearing on ith gear, m (ft)
$L_{N_i} =$	$(L_{o_i} - \delta_{S_i})/L_{1_i}$
L_{o_i}	fully extended strut length of ith gear measured from trunnion attach point to gear axle, m (ft)
L_{1_i}	distance between upper strut trunnion and drag brace upper trunnion measured parallel to strut axis for ith gear, m (ft)
M	Mach number
M_O	mass of the Orbiter, kg (slugs)
P_{DB_i}	drag brace load for ith gear, N (lb)
$\{P\}_j$	load vector from strain gage reading for jth measurement, N (lb)
P_{o_i}	initial pressure in ith strut, N/m^2 (lb/ft^2)
$\bar{q}$	aerodynamic pressure, N/m^2 (lb/ft^2)
$\vec{R}_{\text{cm}}$	vector location of Orbiter c.g., m (ft)
$\vec{R}_{g_i}$	vector location of axle of ith gear from the Orbiter c.g., m (ft)
R_i	undeflected radius of ith gear tire, m (ft)
$\vec{R}_r$	vector location of aerodynamic reference point, m (ft)
$\vec{R}_{t_j}$	vector location of upper trunnion of ith gear from the Orbiter c.g., m (ft)
$\vec{R}_{\text{tire}_i}$	orientation vector of ith tire, m (ft)
r_i	rolling radius of ith tire, m (ft)
S	reference area, m^2 (ft^2)
$\vec{T}_A$	aerodynamic moment vector at reference point, J (ft-lb)
$\vec{T}_{A_{\text{c.g.}}}$	aerodynamic moment vector at c.g., J (ft-lb)
$[T_{BI}]$	Euler angle transformation matrix from body coordinate system to inertial coordinate system
$[T_{EB}]$	transformation matrix from Euler angular rates to body angular rates
TX_A, TY_A, TZ_A	aerodynamic moment vector components at Orbiter c.g. in the body coordinate system, J (ft-lb)
T_x, T_y, T_z	components of total torque on Orbiter, J (ft-lb)
t	time, s
t_f	time when the wheel speed is equal to V_{A_i}, s
t_o	initial time of touchdown, s
V	magnitude of the Orbiter velocity, m/s (ft/s)
V_{A_i}	translational velocity of ith wheel in X_I direction, m/s (ft/s)
V_{A1_i}, V_{B1_i}	trunnion vertical forces on ith gear, N (lb)
V_a	local speed of sound, m/s (ft/s)
V_{head_i}	head volume of ith strut when fully stroked, m^3 (in^3)
V_{s_i}	slip velocity of ith tire, m/s (ft/s)
$\vec{V}_{\text{tire}_i}$	velocity vector of ith tire, m/s (ft/s)
V_x, V_y, V_z	Orbiter velocity components in body coordinate system, m/s (ft/s)
W_x, W_y, W_z	ground-wind velocity components in body coordinate system, m/s (ft/s)

$\ddot{X},\ddot{Y},\ddot{Z}$	Orbiter inertial accelerations, m/s^2 (ft/s^2)
X_B,Y_B,Z_B	orthogonal axes of body coordinate system
X_I,Y_I,Z_I	orthogonal axes of inertial coordinate system
α	angle of attack, deg
β	sideslip angle, deg
δ_a	aileron position, deg
δ_{BF}	body-flap position, deg
δ_e	elevon position, deg
δ_r	rudder position, deg
δ_{S_i}	stroke of ith gear strut, m (ft)
$\dot{\delta}_{S_i}$	stroking velocity of ith strut, m/s (ft/s)
δ_{S_N}	nose gear strut stroke, m (ft)
δ_{S_R}	right main gear strut stroke, m (ft)
δ_{t_i}	deflection of ith tire in Z_I direction, m (ft)
δ_{x_i}	fore-and-aft deflection of ith strut in X_B direction, m (ft)
δ_{y_i}	lateral deflection of ith strut in Y_B direction, m (ft)
$\{\epsilon\}_j$	strain gage vector for jth measurement
$\theta_x,\theta_y,\theta_z$	Euler angles from inertial to body coordinate system, deg
μ_{B_i}	bearing friction coefficient of ith strut
μ_i	drag force friction coefficient of ith tire
μ_{s_i}	side force friction coefficient of ith tire
ρ	local air density, kg/m^3 (slugs/ft^3)
ϕ_i	alinement angle between ith tire orientation and velocity vector, deg
Ω_i	angular velocity of ith wheel about Y_B axis, rad/s
$\omega_x,\omega_y,\omega_z$	angular velocity components of Orbiter, rad/s

Operators:

$(\dot{})$	first derivative with respect to time
$(\ddot{})$	second derivative with respect to time
$(\vec{})$	vector quantity
$(')$	body prime coordinate
$('')$	body double-prime coordinate
$(''')$	body triple-prime coordinate
[ ]	matrix
$[\,]^{-1}$	matrix inverse
$[\,]^T$	matrix or column vector transpose
{ }	set of vectors
$(\hat{})$	unit vector

MATHEMATICAL IDEALIZATION

Coordinate Systems and Transformations

Two coordinate systems are used in the formulation of the mathematical simulation of the Shuttle vehicle touchdown dynamics. Each coordinate system is an orthogonal right-hand set.

Inertial coordinate system (X_I, Y_I, *and* Z_I *axes*).— The inertial coordinate system is defined such that the X_I-Y_I plane forms the landing surface and is assumed to be universally fixed (fig. 1). The Z_I axis is perpendicular to and directed up from the X_I-Y_I plane. The gravity vector is taken to be parallel to the inertial Z_I axis. The equations of motion of the vehicle and landing gear are expressed in the inertial coordinate system.

Body coordinate system (X_B, Y_B, *and* Z_B *axes*).—The body coordinate system is fixed in the Shuttle vehicle so that the origin coincides with the vehicle's center of mass. The body X_B axis is directed along the longitudinal geometric centerline of the vehicle as illustrated in figure 1.

Vehicle geometry, such as landing gear trunnion points, wheel locations, etc., is described by vectors expressed in the body system. The body coordinate system is oriented with respect to the inertial coordinate system by three Euler angles. These angles are produced by three successive rotations about the three body axes in a prescribed order. Associated with a given rotation order is the Euler angle transformation, which transforms vectors in the body system to vectors in the inertial system. This transformation is expressed in matrix form as

$$\begin{Bmatrix} X_I \\ Y_I \\ Z_I \end{Bmatrix} = [T_{BI}] \begin{Bmatrix} X_B \\ Y_B \\ Z_B \end{Bmatrix} \tag{1}$$

where the elements X_I, Y_I, Z_I and X_B, Y_B, Z_B are the inertial and body coordinates, respectively.

The Euler angle rotation sequence that will be used in the development of the Euler angle transformation will be successive rotations about the body X_B axis (θ_x roll), Y_B axis (θ_y pitch), and Z_B axis (θ_z yaw), respectively. The detailed derivation of the Euler transformation and Euler rate transformation is presented in the appendix.

Equations of Motion

The landing configuration of the Shuttle vehicle is idealized as a rigid body of constant mass. Attached to the vehicle are three landing gear assemblies, a nose gear and two main gears (fig. 2). The mass of each landing gear assembly is assumed to be a point mass concentrated at the wheel axle of each assembly. Instead of using the actual mass of the landing gear assembly as the wheel mass, an "effective wheel mass" is computed so that the effective wheel mass located at the wheel axle approximates the inertial characteristics of the landing assembly. Similar assumptions have been made in studies reported in references 1, 2, and 3.

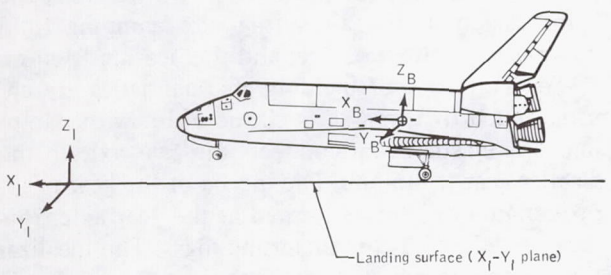

FIGURE 1.—Coordinate system definition.

The rigid vehicle has six degrees of freedom, three in translation and three in rotation. Each landing gear assembly has three degrees of freedom in translation and one degree of freedom in rotation. The three translational equations of motion of the vehicle center of mass are

$$\begin{Bmatrix} \ddot{X} \\ \ddot{Y} \\ \ddot{Z} \end{Bmatrix} = \frac{1}{M_O} \begin{Bmatrix} \Sigma FX \\ \Sigma FY \\ \Sigma FZ \end{Bmatrix} \tag{2}$$

which is a mathematical expression of Newton's second law. The three rotational degrees of freedom are described by the three Euler angles ($\theta_x, \theta_y, \theta_z$) and are related by the three rotational equations of motion (equations (44), (45), and (46) in the appendix).

The rotational equations of motion are functions of the angular rate and angular acceleration vectors and the vehicle inertia. The angular acceleration vector is determined by solving the Euler moment equations or

$$\begin{Bmatrix} T_x \\ T_y \\ T_z \end{Bmatrix} = \begin{bmatrix} I_{xx} & I_{xy} & I_{xz} \\ I_{xy} & I_{yy} & I_{yz} \\ I_{xz} & I_{yz} & I_{zz} \end{bmatrix} \begin{Bmatrix} \dot{\omega}_x \\ \dot{\omega}_y \\ \dot{\omega}_z \end{Bmatrix} + \begin{bmatrix} 0 & -\omega_z & \omega_y \\ \omega_z & 0 & -\omega_x \\ -\omega_y & \omega_x & 0 \end{bmatrix} \begin{bmatrix} I_{xx} & I_{xy} & I_{xz} \\ I_{xy} & I_{yy} & I_{yz} \\ I_{xz} & I_{yz} & I_{zz} \end{bmatrix} \begin{Bmatrix} \omega_x \\ \omega_y \\ \omega_z \end{Bmatrix} \tag{3}$$

Using an appropriate integration scheme, the solution of the vehicle equation of motion will yield the time histories of the characteristic parameters.

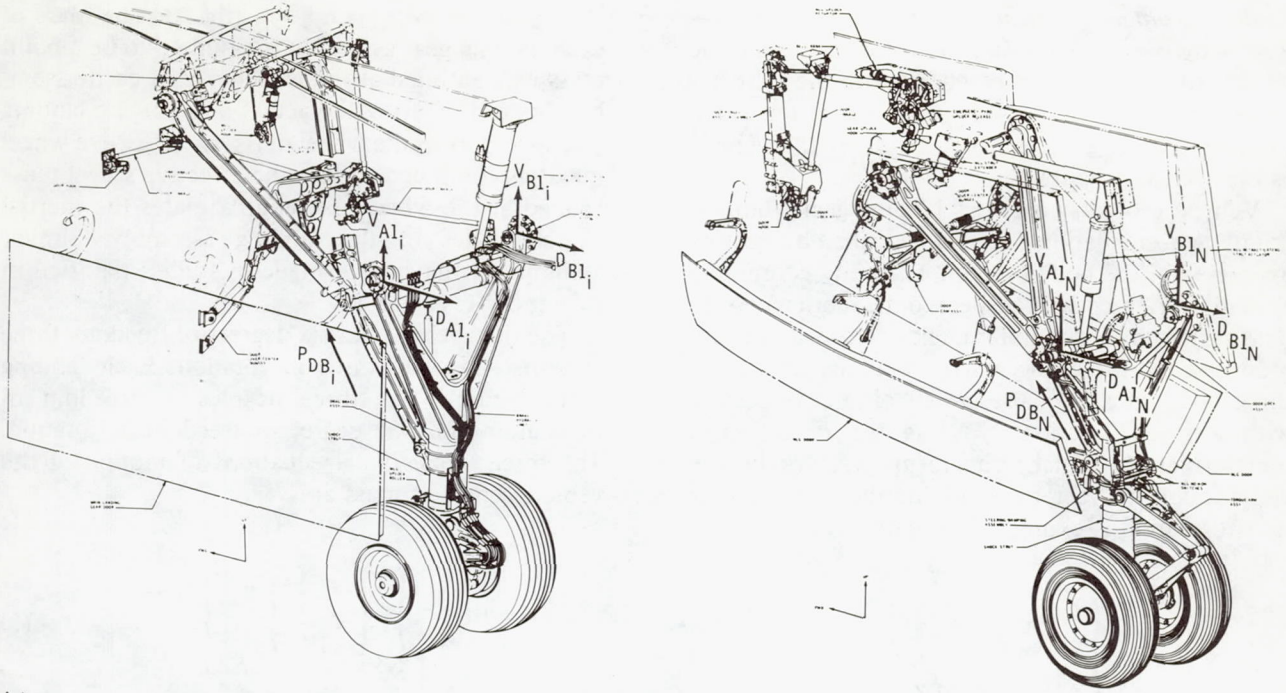

(a) (b)

FIGURE 2.—Landing gear chassis assembly. (a) Main landing gear. (b) Nose landing gear.

Landing Gear Forces

The Orbiter landing gear configuration is a tricycle type with primary braking on the main wheels. During landing impact, the vertical motion of the Orbiter is arrested through the compression of the oleo-pneumatic struts and tires of the landing gear system.

The landing gear forces that are critical to the Orbiter structural design are those associated with the landing gear wheel "spin-up" and "spring-back" phenomenon that occurs during gear impact. As the aircraft approaches the landing site, the rotation speed Ω_i of the gear wheels is approximately zero. As the wheels make contact with the landing surface, the friction between the tires and the surface causes the wheels to rotate. The frictional forces increase the rotational speed of the wheel until it is synchronous with the translational velocity of the gear axle V_{A_i}.

Because of the elasticity of the gear, the frictional forces will cause the landing gear strut to deflect. At some point in the aft deflection of the strut, the landing gear trunnion forces will be at a maximum. This point is defined as the maximum spin-up load. The subsequent rebound of the strut will cause a reversal in loading in the gear upper trunnions. This reversal in loading is defined as the spring-back load. Usually the spin-up and spring-back loads are at a maximum during the first bending oscillatory cycle.

The landing gear forces during initial impact are governed by the tire compression modulus. During this phase, the tire load increases with deflection until the force component along the strut axis is greater than the preload in the strut, at which time the gear will begin to stroke. Prior to this, the oleo-pneumatic strut will remain fully extended. The magnitude of the strut preload is set by the initial internal pressure of the strut air spring. As the tire load exceeds the strut preload, the strut will start to stroke. The strut stroking forces are due primarily to the nonadiabatic compression of the air spring, the damping fluid moving through an orifice, and the bearing friction.

The landing gear bending characteristics are approximated by a massless elastic beam with damping. The elastic beam connects the gear axle to the Orbiter gear trunnions. The inertia of the gear is approximated by a mass located at the gear axle; this mass is defined as the unsprung mass. The idealization of the gear is pictorially presented in figure 3. The unsprung mass is given four degrees of freedom,

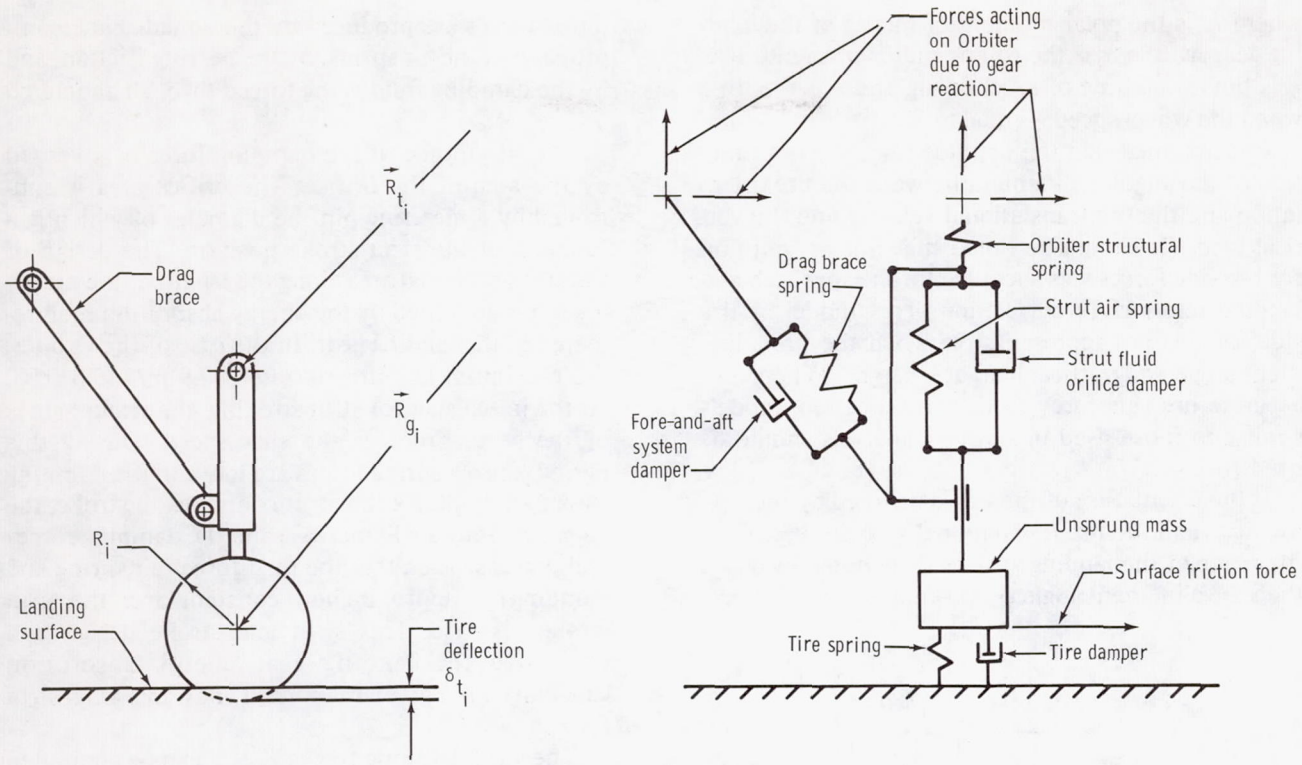

FIGURE 3.—Landing gear idealization.

three in translation and one in rotation. The rotational degree of freedom is associated with the spin-up phenomenon of the wheel assembly during the initial touchdown phase. The vectors $\vec{R}_{t_i}$ and $\vec{R}_{g_i}$ define the positions of the upper trunnion and gear wheel axle, respectively.

The forces acting on the unsprung mass can be divided into ground reaction forces and strut forces. The orthogonal components of the ground reaction forces are (1) vertical force F_{v_i}, (2) drag force F_{D_i}, and (3) side force F_{ϕ_i}. The side and drag forces are assumed to be in the plane of the landing surface. Similarly, the strut forces are due to the strut stroking dynamics and strut bending. The strut bending forces are orthogonal to the longitudinal axis of the strut and act at the wheel axle.

Tire/ground forces.—The tire vertical ground forces are a function of the tire deflection δ_{t_i} and deflection rate $\dot{\delta}_{t_i}$ and are computed by

$$F_{v_i} = K_{\text{tire}_i}\delta_{t_i} + K_{RT_i}\dot{\delta}_{t_i} \tag{4}$$

where K_{tire_i} is the nonlinear elastic modulus of the tire and K_{RT_i} is the nonlinear damping coefficient of the tire. During wheel spin-up, the friction force acting on the tire is a function of the vertical load F_{v_i} and the slip velocity V_{s_i}. From experimental data, the friction coefficient μ_i between the tire and the landing surface is developed as a function of the slip velocity. Generally, the friction coefficient is at a maximum when the wheel rotational velocity is approximately 80 to 90 percent of the axle translational velocity. The drag force F_{D_i} on the tire is computed by

$$F_{D_i} = \mu_i F_{v_i} \tag{5}$$

The slip velocity is given by the solution of the integral equation

$$V_{s_i} = V_{A_i} - \int_{t_o}^{t_f} \frac{F_{D_i} r_i}{I_{p_i}}\, dt \tag{6}$$

where I_{p_i} is the polar moment of inertia of the landing gear wheels, r_i is the rolling radius of the ith tire, t_0 is the initial time of touchdown, and t_f is the time when the wheel speed is equal to V_{A_i}.

It is assumed that the tire side force F_{ϕ_i} is a function of the angular alinement between the tire orientation and the tire translational velocity and the vertical load. (It should be noted that this assumption for tire side forces was adequate for the approach and landing test (ALT) correlation. This model of tire side force is not representative when the tire alinement angle and vertical load are "large." When very accurate tire side force models are required, models similar to those used in shimmy analysis should be used (ref. 4).)

If the orientation of the tire is denoted by the vector $\vec{R}_{\text{tire}_i}$ and the tire translational velocity vector, in the plane of the landing surface, is denoted by $\vec{V}_{\text{tire}_i}$, then the alinement angle ϕ_i is computed by

$$\phi_i = \cos^{-1}\left[\frac{\vec{R}_{\text{tire}_i} \cdot \vec{V}_{\text{tire}_i}}{\left|\vec{R}_{\text{tire}_i}\right| \cdot \left|\vec{V}_{\text{tire}_i}\right|}\right] \tag{7}$$

The tire force, acting normal to the tire orientation vector $\vec{R}_{\text{tire}_i}$, normally increases when the magnitude of the alinement angle increases to the point of tire skidding.

The side force is also dependent on the magnitude of the tire vertical load F_{v_i}. From experimental data, the side force friction coefficient μ_{s_i} can be expressed as a linear function of the tire alinement angle ϕ_i. Under this assumption, the side force F_{ϕ_i} is computed by

$$F_{\phi_i} = \mu_{s_i} F_{v_i} \tag{8}$$

The coefficient μ_{s_i} is normally developed from experimental data and is presented as a function of the alinement angle ϕ_i. The side friction coefficient μ_{s_i} is approximately linear with the alinement angle to approximately 10°. Alinement angles greater than 10° produce quasi-skidding conditions in the tires, resulting in a reduction in tire side force.

Strut forces.—The oleo-pneumatic strut attenuates the landing forces through the mechanism of strut compression. During the compression, the strut internal forces are produced by the nonadiabatic compression of the air spring, by the bearing friction, and by the damping fluid being forced through a metered orifice.

The magnitude of the damping force is governed by the area of the orifice. The orifice area is controlled by a metering pin the diameter of which is a function of the strut stroke position. The design of the cross-sectional area along the length of the metering pin is governed by the energy absorption requirements of the landing gear. In the case of the Orbiter, the maximum design sink rate is 2.9 m/s (9.6 ft/s). At the initial stage of strut stroking, the stroke rate is of the same order as the sink speed. During this period, the air spring forces are low and the damping forces are high. As the strut continues to stroke, the air spring forces will increase and the damping forces will decrease such that the total force (air spring and damping) is approximately constant over the strut stroke distance. This strut load-stroke design will maximize the landing gear energy absorption capability for a given maximum allowable axial strut force.

The strut damping forces F_{damp_i} can be computed by

$$F_{\text{damp}_i} = C_{\text{damp}_i} \dot{\delta}_{S_i} \frac{\dot{\delta}_{S_i}}{\left|\dot{\delta}_{S_i}\right|} \tag{9}$$

where $\dot{\delta}_{S_i}$ is the strut stroking velocity and C_{damp_i} is the nonlinear damping coefficient, which is a function of the strut stroke. The strut air spring force F_{air_i} can be computed by

$$F_{\text{air}_i} = P_{o_i} A_{\text{piston}_i}^{1-K_i} \left[\frac{V_{\text{head}_i}}{\frac{V_{\text{head}_i}}{A_{\text{piston}_i}} - \delta_{S_i}}\right]^{K_i} \tag{10}$$

where P_{o_i} is the initial static internal strut pressure, A_{piston_i} is the strut piston cross-sectional area, V_{head_i} is the head volume of the strut when fully stroked, and K_i is the polytropic gas constant.

The strut bending forces are reacted internally by two bearings: the lower bearing, which is fixed to the

upper section of the strut, and the upper bearing, which is fixed to the stroking segment of the strut. The bearing reaction forces F_{B1_i} and F_{B2_i} are illustrated in figure 4. The bearing reaction forces are computed by

$$F_{B1_i} = F_{\text{bend}_i}\left[\frac{L_i}{L_{b_i} + \delta_{S_i}}\right] \tag{11}$$

and

$$F_{B2_i} = F_{\text{bend}_i}\left[\frac{L_i}{L_{b_i} + \delta_{S_i}} - 1\right] \tag{12}$$

where L_i is the strut length from the axle to the upper bearing and L_{b_i} is the length between the two bearings when the gear is fully extended.

The bearing friction force F_{Br_i} present when the gear is stroking is given by

$$F_{Br_i} = \mu_{B_i}\left[\left|F_{B1_i}\right| + \left|F_{B2_i}\right|\right]\frac{\dot{\delta}_{S_i}}{\left|\dot{\delta}_{S_i}\right|} \tag{13}$$

where μ_{B_i} is the bearing friction coefficient at the upper and lower strut bearings. It should be noted that these bearing friction forces are present only in a dynamic condition; special care should be taken when programing these equations for the digital computer to ensure that these forces are not computed while in a static condition.

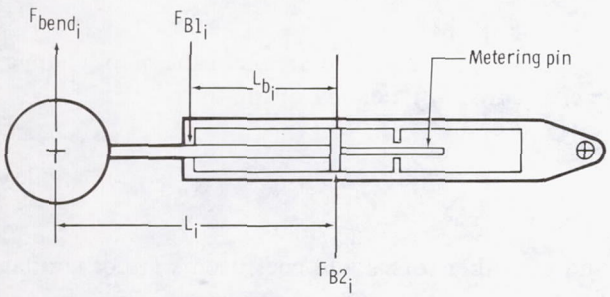

FIGURE 4.—Bearing load illustration for fully extended gear.

The net axial strut force F_{strut_i} is the summation of the components or

$$F_{\text{strut}_i} = F_{Br_i} + F_{\text{air}_i} + F_{\text{damp}_i} \tag{14}$$

The strut bending force F_{bend_i} acts normal to the strut axial force and is located at the wheel axle. The bending forces are divided into side-to-side bending and fore-and-aft bending. The magnitude of the strut bending forces can be related to the strut bending stiffness, bending deflection, and deflection rate. The bending deflection from side to side and the deflection rate will be denoted by δ_{y_i} and $\dot{\delta}_{y_i}$, respectively. Similarly, the fore-and-aft deflection and the deflection rate are δ_{x_i} and $\dot{\delta}_{x_i}$, respectively.

The fore-and-aft bending motion of the gear can be described by idealizing the gear, in the x direction, as a beam supported by a pinned joint at the upper trunnion point and a pinned joint at the drag brace attachment. An effective bending stiffness EI_{x_i} is assumed. It is also assumed that the drag brace stiffness can be approximated by a linear spring of stiffness K_{b_i}. Under these assumptions, the fore-and-aft bending force F_{Bx_i} is

$$F_{Bx_i} = C_{Bx_i}\dot{\delta}_{x_i} + \frac{\delta_{x_i}}{\left[\frac{L_{N_i}^2}{K_{b_i}} + \frac{L_{1_i}^3}{3EI_{x_i}}\left(L_{N_i}^3 - 2L_{N_i}^2 + L_{N_i}\right)\right]} \tag{15}$$

where

$$L_{N_i} = \frac{\left(L_{o_i} - \delta_{S_i}\right)}{L_{1_i}} \tag{16}$$

L_{o_i} is the initial strut length, L_{1_i} is the distance between the strut upper trunnions and the drag brace attachment to the strut, C_{Bx_i} is the fore-and-aft damping coefficient, and EI_{x_i} is the average fore-and-aft bending stiffness.

The side-to-side bending motion of the gear can be described by idealizing the gear, in the y direction, as a cantilever beam with an effective bending stiffness

EI_{y_i}. Under these assumptions, the bending force in the y direction is

$$F_{By_i} = \frac{3EI_{y_i}}{\left(L_{o_i} - \delta_{S_i}\right)^3} \delta_{y_i} + C_{By_i} \dot{\delta}_{y_i} \qquad (17)$$

where C_{By_i} is the side-to-side damping coefficient. The net bending force F_{bend} used in the calculation of the bearing forces is

$$F_{\text{bend}_i} = \sqrt{F_{Bx_i}^2 + F_{By_i}^2} \qquad (18)$$

With the forces acting on the gear unsprung mass defined by equations (4), (5), (8), (14), (15), and (17), the accelerations of the unsprung mass can be computed. Using an appropriate numerical integration scheme, the time history of the position vector $\vec{R}_g$ can be determined. The landing gear forces acting on the Orbiter are assumed to be opposite and equal to those strut forces acting on the unsprung mass.

Aerodynamic Forces

Aerodynamic forces and moments acting on the Orbiter during landing are computed as a function of angle of attack, sideslip angle, Mach number, dynamic pressure, reference area, control surface positions, and aerodynamic coefficients.

The angle of attack α (ref. 5) is computed from the Orbiter velocity vector and the local winds; i.e.,

$$\alpha = \tan^{-1}\left(\frac{V_z - W_z}{V_x - W_x}\right) \qquad (19)$$

where V_z and V_x are components of the Orbiter airspeed in the Orbiter coordinate system and W_x and W_z are the crosswind components in the same system. Similarly, the sideslip angle β is computed by

$$\beta = \sin^{-1}\left(\frac{V_y - W_y}{V}\right) \qquad (20)$$

where

$$V = \sqrt{(V_x - W_x)^2 + (V_y - W_y)^2 + (V_z - W_z)^2} \qquad (21)$$

The Mach number M is defined by

$$M = \frac{V}{V_a} \qquad (22)$$

where V is the magnitude of the Orbiter velocity and V_a is the local speed of sound.

The dynamic pressure $\bar{q}$ is computed by

$$\bar{q} = \frac{1}{2}\rho V^2 \qquad (23)$$

where ρ is the local air density.

The Orbiter autoland control system is modeled in this analysis according to its description in reference 6. The control system determines control surface deflections as a function of Orbiter attitudes, angular rates, dynamic pressure, runway position, load factors, horizontal velocity, and gear deflection. The surfaces include the elevons, ailerons, rudder, speed brakes, and body flaps.

Aerodynamic data for the Orbiter landing configuration are described in reference 7. These nonlinear data are used in these analyses in tabular form as a function of the aforementioned parameters.

Thus, the six-degree-of-freedom aerodynamic forces and moments (FX_A, FY_A, FZ_A, TX_A, TY_A, and TZ_A) are computed by equations of the form

$$FX_A = Cx\bar{q}S \qquad (24)$$

where S is the reference area and the aerodynamic coefficient is functionally of the form

$$Cx = f(\alpha, \beta, M, \delta_e, \delta_a, \delta_r, \delta_{SB}, \delta_{BF}) \qquad (25)$$

and the other forces and coefficients are of similar form.

The forces $\vec{F}_A$ and the moments $\vec{T}_A$ are transferred from the reference point to the center of gravity (c.g.) by

$$\vec{F}_{A_{c.g.}} = \vec{F}_A \tag{26}$$

and

$$\vec{T}_{A_{c.g.}} = \vec{T}_A + \left(\vec{R}_r - \vec{R}_{cm}\right) \times \vec{F}_A \tag{27}$$

These are the aerodynamic forces and moments acting on the Orbiter that drive the Euler moment equations and the Newton translational equations.

GEAR INSTRUMENTATION

The main and nose landing gears on Orbiter vehicle 101 were instrumented with strain gages on the lower drag link, the upper strut trunnion pins, and the strut/wheel torque link mechanism (fig. 5). The strain gages all had a frequency response of 0 to 50 hertz. The four gages on the lower drag brace were mounted on an I-beam section of the brace and the output of the four gages was electrically averaged to obtain the resulting tensile or compressive strain. The strut trunnion pins were hollow cylinders with four gages mounted on the inner surface. The outputs of the upper and lower gages on the pins were combined to obtain drag load and the outputs of the forward and aft gages were combined to obtain vertical load. Differential vertical loads between the inboard and outboard trunnions were used to obtain side loads. Each side of the main gear torque link mechanism was instrumented with a strain gage. The output of these two gages was combined to obtain strut torque.

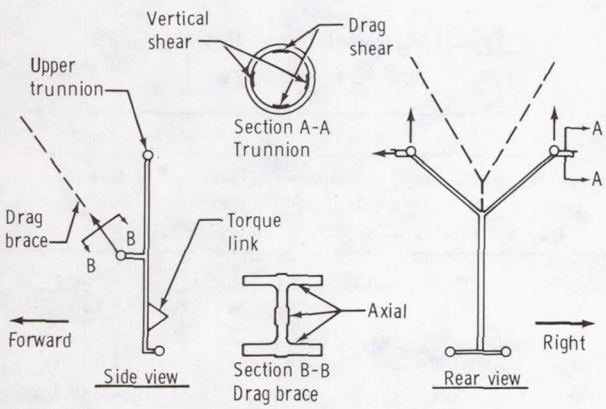

FIGURE 5.—Main and nose gear strain gage schematic.

Each gear was also instrumented with a stroke measurement device and with wheel-speed sensors. All the above data were recorded on a wide-band recorder at a sample rate of 400 samples per second. This type of sample rate provided a good resolution of gear loading during the landing phase.

LANDING GEAR CALIBRATION

The main and nose landing gears were load calibrated using a system calibration technique.[1,2] This calibration involved applying various combinations of vertical, drag, and side loads and torques to the gear at the axle as shown in figure 6 and then recording the strain gage outputs for each load condition. The load combinations were applied in incremental percentages of 20, 40, 60, 80, and 100 percent of maximum load so that repeatability and linearity of the strain gage output could be established.

The resulting set of load and output data was used in a "least-squares" solution to develop calibration constants for each gear. These calibration constants represent a linear relation between strain gage output and the corresponding gear loads. This relation is of the form

$$\{P\}_j = [C]_j \{\epsilon\}_j \tag{28}$$

where $\{\epsilon\}_j$ are strain gage readings, $[C]_j$ are the calibration constants, and $\{P\}_j$ are the corresponding loads. The constants $[C]_j$ for the left main, right main, and nose gears are given in figure 7 and are taken from internal data.[1-3] The strut was calibrated

[1]A. L. Carter, "OV-101 Landing Gear Calibration Results," NASA Dryden Flight Research Center Internal Letter, July 1977.

[2]A. L. Carter, "OV-101 Landing Gear Post Flight Strain Gage Hookup and Sensitivity Checks," NASA Dryden Flight Research Center Internal Letter, Jan. 1978.

[3]Walter B. Horne, "Tire Friction Coefficient Estimates for Decelerating and Steering the Space Shuttle Vehicle During Landing on Conventional, Grooved, and Lakebed Surfaces," NASA Langley Research Center Internal Letter, Nov. 5, 1976.

by stroking the strut in incremental amounts from fully extended to fully stroked and recording the electrical output of the linear potentiometer for each strut position. The wheel-speed sensors were calibrated in a laboratory but not on the gear assembly. However, their apparent accuracy was satisfactory.

LANDING LOADS AND CORRELATION

Correlation with the ALT loads was done for both main and nose gear impact and for occurrence of maximum main gear tire loads. In general, the strain gage output from the right main gear was more consistent than that from the left main gear and thus was considered more representative of the actual loads.

The horizontal velocity and sink rates at both main and nose gear impact for each ALT flight are shown in table I. The main gear loads for free flight 5 (FF5) were the highest of all flights because of the high sink rate, whereas the nose gear loads were the highest for FF2. However, for nose gear correlation, FF5 loads were used because the FF5 flight represented the actual Orbiter tail-cone-off configuration. The maximum main gear tire loads occurred on FF4 because of the high horizontal velocity at nose gear impact, which produced a high downward aerodynamic load on the Orbiter and thus a high tire load.

As shown in the sections on tire/ground loads and strut loads, the forces acting on the gear strut at the axle can be calculated as a function of time. The corresponding loads acting at the gear trunnions, as illustrated in figure 7, can be resolved from the loads at the axle using the gear geometry. The trunnion loads and the drag brace loads are used for correlation because they are directly proportional to the strain gage measurements.

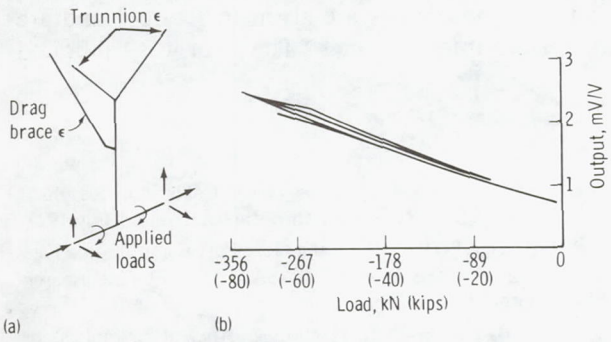

FIGURE 6.—Calibration test data. (a) Sketch showing applied loads. (b) Typical strain gage output (vertical load, inboard trunnion, right main gear).

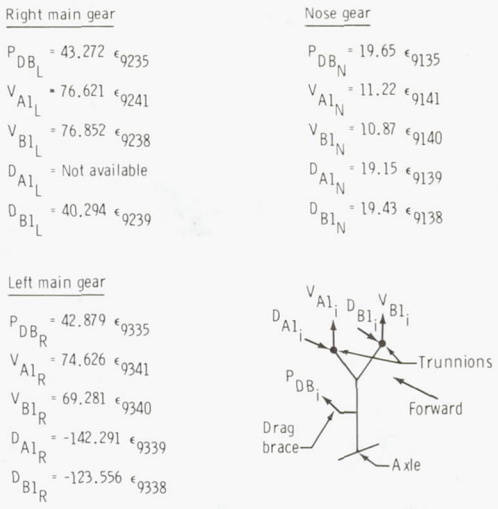

FIGURE 7.—Main and nose gear calibration constants.

The main gear impact loads on the right main lower drag brace and upper strut trunnion for FF5 are shown in figure 8. The location of these loads is given in figure 7. Also shown with the measured loads are the predicted loads using the pre-ALT main gear math model. These three loads were used for correlation because they were largest in magnitude and all other ground reaction and trunnion loads can be calculated from them. The correlation between analysis and test was good for these loads. However, a refinement of strut bending damping and gear unsprung mass produced excellent correlation as shown in figure 9. The remaining differences between analysis and test are attributed to inaccuracies in initial conditions, data measurement, and mathematical modeling. The right main strut stroke for the

TABLE I.— Horizontal and Vertical Velocities for ALT Landings

Flight	Main gear impact		Nose gear impact	
	Horizontal velocity, m/s (knots)	Sink rate, m/s (ft/s)	Horizontal velocity, m/s (knots)	Sink rate, m/s (ft/s)
1	99 (192)	−0.3 (−1.0)	76 (148)	1.3 (4.2)
2	96 (186)	−.3 (−1.0)	70 (137)	2.1 (6.8)
3	99 (192)	−.3 (−.9)	77 (150)	1.3 (4.3)
4	102 (199)	.9 (3.0)	84 (163)	1.0 (3.3)
5	78 (152)	[a]2.0 (6.5)	68 (132)	2.0 (6.4)

[a]Second impact.

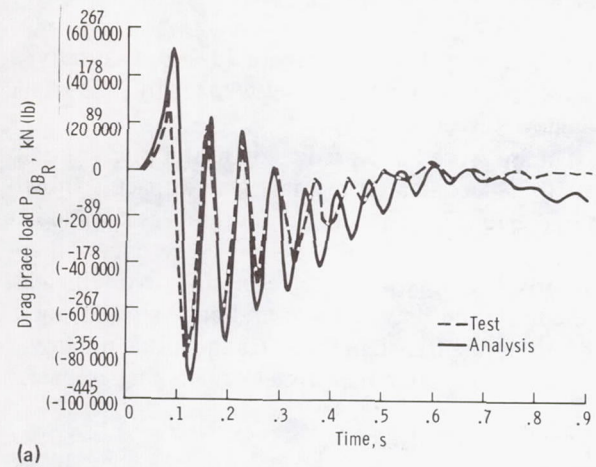

(a)

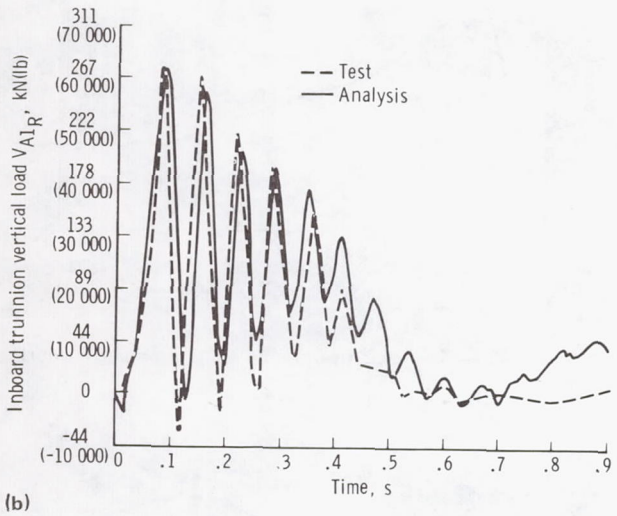

(b)

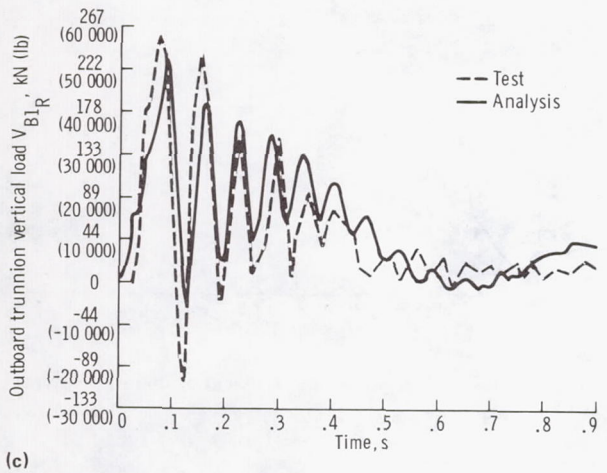

(c)

FIGURE 8.—Right main landing gear loads and correlation using pre-ALT math model. (a) Drag brace. (b) Inboard trunnion, vertical load. (c) Outboard trunnion, vertical load.

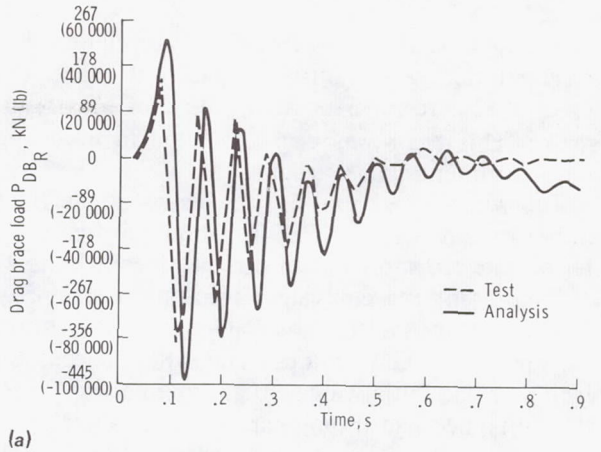

(a)

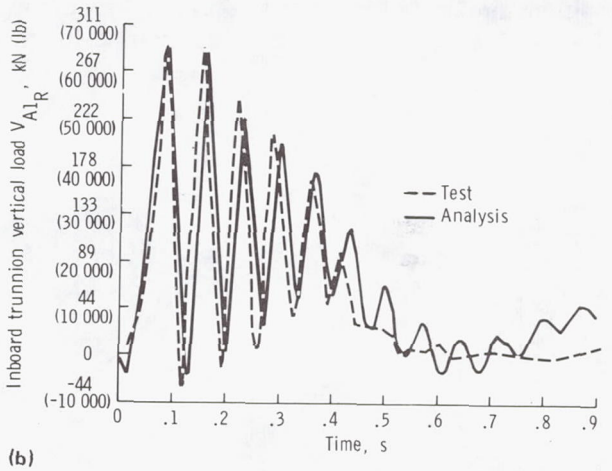

(b)

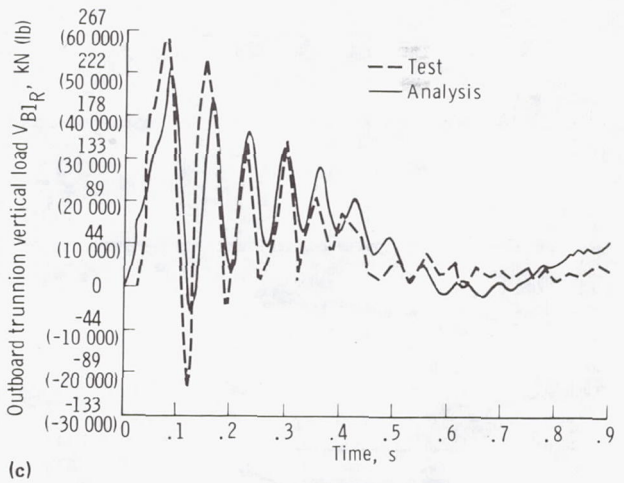

(c)

FIGURE 9.—Right main landing gear loads and correlation using updated math model. (a) Drag brace. (b) Inboard trunnion, vertical load. (c) Outboard trunnion, vertical load.

FF5 landing is shown in figure 10. Correlation was excellent during the initial impact but there was about a 10-percent error at the time of maximum stroke. This error was also attributed to modeling and instrumentation inaccuracies.

The wheel-speed spin-up transients for the right and left main gears for FF5 are shown in figure 11. These data are shown in meters per second (knots) and represent the equivalent translational velocity that corresponds to the wheel angular velocity times the apparent rolling radius. The wheel speeds on each gear had initial values of approximately 30 m/s (60 knots) because of their partial spin-up on the previous gear contact which occurred on FF5. Correlation was within 10 percent on magnitude and within 20 percent on timing. It should be noted that the spin-up timing is very sensitive to the tire/ground friction coefficient. The friction curve used for the FF5 landing is shown in figure 12 and was derived from friction data measurements made by the NASA Langley Research Center.[3]

The measured and predicted Orbiter pitch rate on FF5 for 1 second after primary gear impact is shown in figure 13. The measured pitch rate was sampled at a much lower rate than the strain gage data and apparently had less accurate resolution. Nonetheless, the correlation between test and analysis was good. The pitch rate transient indicates the initial pitchover of the Orbiter after the primary main gear impact.

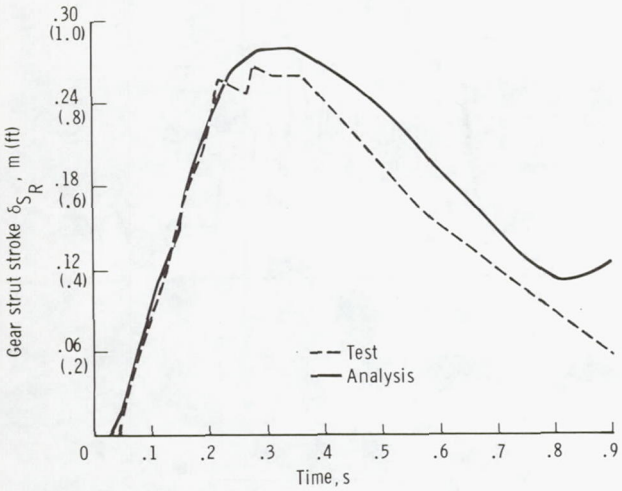

FIGURE 10.—Right main gear strut stroke for main gear impact on FF5.

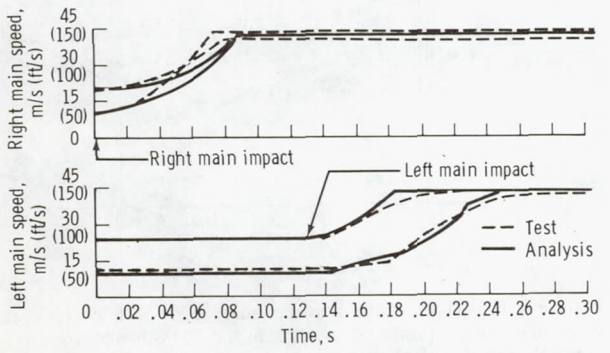

FIGURE 11.—Main gear wheel speed during impact on FF5.

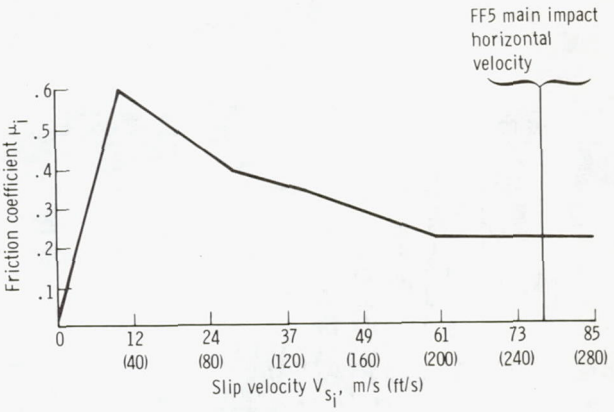

FIGURE 12.—Main gear tire/ground friction properties during spin-up.

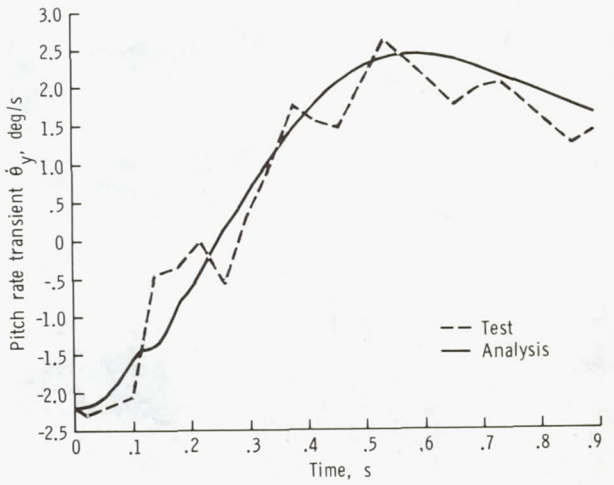

FIGURE 13.—Orbiter pitch rate transient at main gear impact on FF5.

[3]Walter B. Horne, "Tire Friction Coefficient Estimates for Decelerating and Steering the Space Shuttle Vehicle During Landing on Conventional, Grooved, and Lakebed Surfaces," NASA Langley Research Center Internal Letter, Nov. 5, 1976.

Nose gear impact loads on the lower drag brace and upper strut trunnion for FF5 are shown in figure 14, together with the predicted loads using the pre-ALT nose gear mathematical model. Only one of the Z trunnion loads is shown because the inboard and outboard loads are very similar. The correlation between analysis and test was fairly good; however, refinements in the nose gear unsprung mass produced very good correlation as shown in figure 15. The remaining differences between analysis and test are attributed to the same type inaccuracies as for the main gear. The nose gear stroke at nose gear impact for FF5 is shown in figure 16. As in the case of the main gear, the stroke correlation is excellent during initial impact but has an error of about 11 percent at the time of maximum stroke. This error is again attributed to instrumentation, calibration, and modeling inaccuracies.

The maximum main gear tire loads for each ALT flight are shown in table II. Also shown are the corresponding horizontal velocity and elevon position for each flight. These loads were calculated from the drag brace and trunnion loads. These tire loads correspond to a 50-50 distribution of the total ground reaction to each tire. There was no instrumentation to discern differential tire loads on each gear. The predicted tire loads for each flight showed good agreement, with a maximum error of 13.8 percent on FF5. This type of error was within the tolerance band of measurements and flight conditions. As previously noted, the tire loads on FF4 were the highest of all ALT landings.

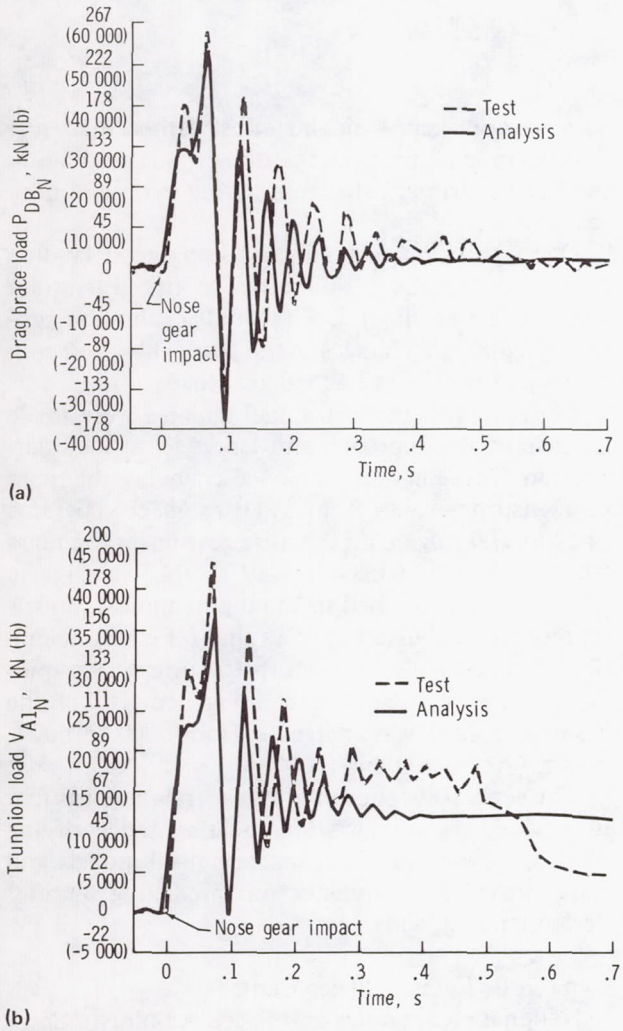

FIGURE 14.—Nose gear loads and correlation for FF5 using pre-ALT math model. (a) Drag brace. (b) Trunnion (left).

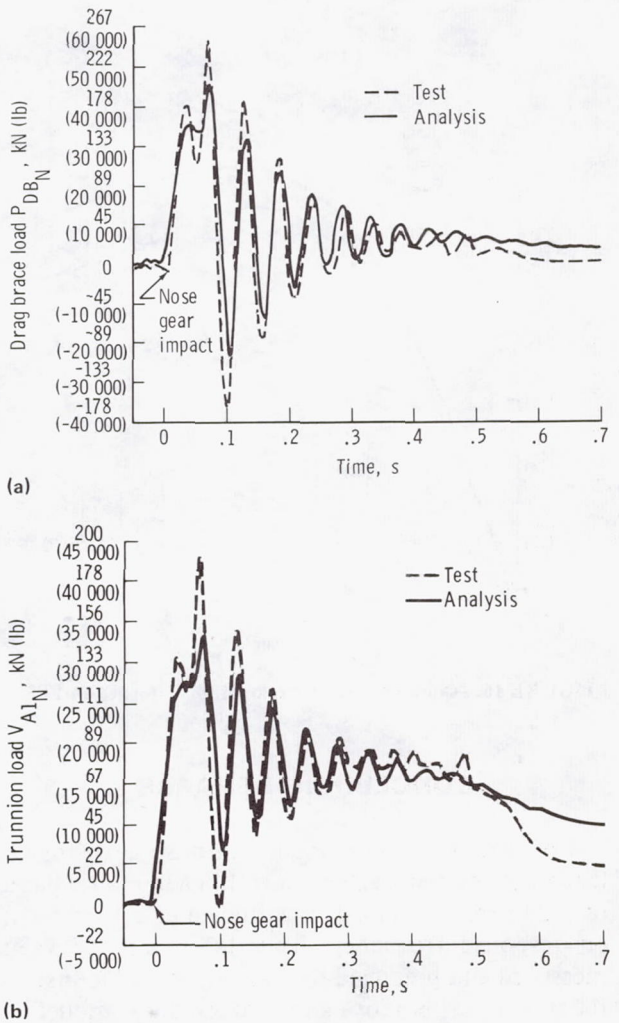

FIGURE 15.—Nose gear loads and correlation for FF5 using updated math model. (a) Drag brace. (b) Trunnion (left).

TABLE II.— Maximum Main Gear Tire Loads for ALT

Flight	Main gear tire load, N (lb)								Horizontal velocity, m/s (knots) (a)	Elevon position (a)
	Right gear				Left gear					
	Measured		Predicted		Measured		Predicted			
				With tail cone on						
1	311 800	(70 100)	321 600	(72 300)	377 600	(75 900)	321 600	(72 300)	76.1 (148.0)	−33°
2	299 800	(67 400)	298 000	(67 000)	—	—	298 000	(67 000)	70.4 (136.8)	−33°
3	297 600	(66 900)	325 600	(73 200)	338 100	(76 000)	325 600	(73 200)	77.0 (149.7)	−33°
				With tail cone off						
4	330 500	(74 300)	338 100	(76 000)	366 500	(82 400)	338 100	(76 000)	83.8 (162.8)	−16°
5	244 200	(54 900)	278 000	(62 500)	253 500	(57 000)	278 000	(62 500)	67.4 (131.1)	−12°

[a]At time of maximum load.

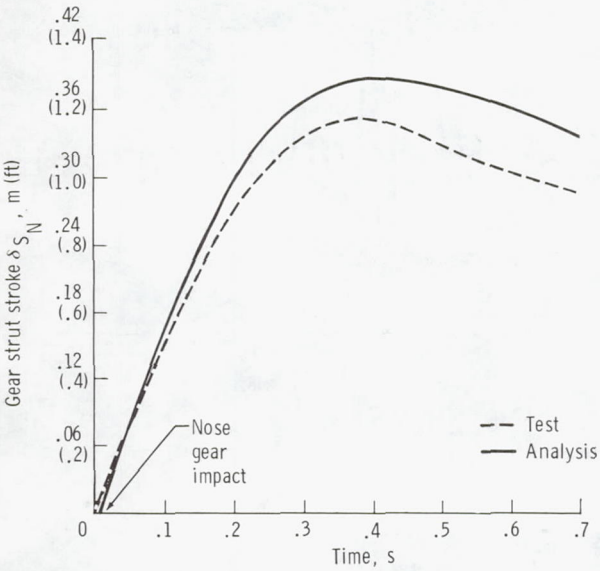

FIGURE 16.—Nose gear strut stroke at nose impact on FF5.

CONCLUDING REMARKS

Correlation between main and nose gear impact loads was generally achieved within a tolerance band of ±20 percent on load magnitude and ±10 percent on response frequency. The differences between measured and predicted data are attributed to instrumentation, calibration, and mathematical modeling inaccuracies. It should be noted that both magnitude and phasing were important in this correlation because gear load time histories, rather than just maximum load, produce the design-type loading on the Orbiter primary structure during main and nose gear impact.

One significant factor in obtaining good landing loads was the shunt calibration of the gear strain gages after free flight 5. The shunt calibration produced significant changes in the gear calibration constants and thus in the actual gear loads.

Certain mathematical model updates were made because of the approach and landing test load correlation. These updates included changing the main gear unsprung mass from 594.0 to 685.9 kilograms (40.7 to 47.0 slugs) and the nose gear unsprung mass from 144.5 to 211.6 kilograms (9.9 to 14.5 slugs). The unsprung mass as used in the mathematical models represents an equivalent mass that reflects acceleration of the gear and its support structure during spin-up/spring-back. Also, the bending damping of the main gear strut was increased from 3000 to 6000 N-s/m (200 to 400 lb-s/ft).

The general conclusion of this correlation was that it provided a good basis for updating and verifying main and nose gear loads mathematical models and thus provided confidence in predicting Orbiter design landing loads.

Lyndon B. Johnson Space Center
National Aeronautics and Space Administration
Houston, Texas, September 28, 1979
986-15-31-05-72

REFERENCES

1. Mantus, M.; Lerner, E.; and Elkins, W.: Landing Dynamics of the Lunar Excursion Module (Method of Analysis). Rep. LED-520-6, Grumman Aircraft Engineering Corp., Mar. 6, 1964.

2. Holder, Ben Walton: A Study of the Effect of Landing Gear Mass and Inertia on Spacecraft Touchdown Stability. M.S. Thesis, University of California, Los Angeles, 1966.

3. Zupp, George A., Jr.; and Doiron, Harold H.: A Mathematical Procedure for Predicting the Touchdown Dynamics of a Soft-Landing Vehicle. NASA TN D-7045, 1971.

4. Bourcier de Carbon, Christian: Analytical Study of Shimmy of Airplane Wheels and Landing Gear. NACA TM-1337, Sept. 1952.

5. Etkin, Bernard: Dynamics of Flight—Stability and Control. John Wiley and Sons, Inc. (New York), 1959, pp. 10-11.

6. Space Shuttle Orbital Flight Test Level C Functional Subsystem Software Requirements: Guidance, Navigation, and Control; Part C, Flight Control-Entry. Rep. SD76-SH-0007A, Rockwell International Space Division, May 31, 1978.

7. Aerodynamic Design Data Book, Volume 1, Orbiter Vehicle 102. Rep. SD72-SH-0060, Vol. 1K, Rockwell International Space Division, Nov. 1977.

APPENDIX

DERIVATION OF THE EULER TRANSFORMATION

An Euler transformation transforms vectors from a body coordinate system to an inertial coordinate system. Consider the origin of the body coordinate system (X_B, Y_B, Z_B) to be located at the center of mass of the vehicle and to be initially alined with the inertial coordinate system (X_I, Y_I, Z_I) as shown in figure 17. (Both coordinate systems are orthogonal.) The Z_I axis is directed upward and is parallel to the gravity vector, and the X_I-Y_I axes define the plane of the landing surface (fig. 17(a)).

The body coordinate system is oriented with respect to the inertial coordinate system by the set of Euler angles θ_x, θ_y, and θ_z. With respect to the vehicle, θ_x represents the roll angle, θ_y the pitch angle, and θ_z the yaw angle. The Euler transformation will be developed for the rotation sequence of roll, pitch, and yaw, with each successive rotation taken about the indicated body axis.

The first Euler angle θ_x is developed by rotating the body about the X_B axis. For this configuration (fig. 17(b)), a body prime coordinate system (X'_B, Y'_B, Z'_B) is introduced. The transformation that transforms vectors in the body prime system to vectors in the inertial system is given by

$$\begin{Bmatrix} X_I \\ Y_I \\ Z_I \end{Bmatrix} = \begin{bmatrix} 1 & 0 & 0 \\ 0 & \cos\theta_x & -\sin\theta_x \\ 0 & \sin\theta_x & \cos\theta_x \end{bmatrix} \begin{Bmatrix} X'_B \\ Y'_B \\ Z'_B \end{Bmatrix} \tag{29}$$

The second Euler angle θ_y is developed by rotating the body about the Y'_B axis. For this configuration (fig. 17(c)), a body double-prime coordinate system (X''_B, Y''_B, Z''_B) is introduced. The transformation that transforms vectors in the body double-prime system to vectors in the prime system is given by

$$\begin{Bmatrix} X'_B \\ Y'_B \\ Z'_B \end{Bmatrix} = \begin{bmatrix} \cos\theta_y & 0 & \sin\theta_y \\ 0 & 1 & 0 \\ -\sin\theta_y & 0 & \cos\theta_y \end{bmatrix} \begin{Bmatrix} X''_B \\ Y''_B \\ Z''_B \end{Bmatrix} \tag{30}$$

The third and final Euler angle θ_z is developed by rotating the body about the Z''_B axis. For this configuration (fig. 17(d)), a body triple-prime coordinate system (X'''_B, Y'''_B, Z'''_B) is introduced. The transformation that transforms vectors in the body triple-prime system to vectors in the double-prime system is given by

$$\begin{Bmatrix} X''_B \\ Y''_B \\ Z''_B \end{Bmatrix} = \begin{bmatrix} \cos\theta_z & -\sin\theta_z & 0 \\ \sin\theta_z & \cos\theta_z & 0 \\ 0 & 0 & 1 \end{bmatrix} \begin{Bmatrix} X'''_B \\ Y'''_B \\ Z'''_B \end{Bmatrix} \tag{31}$$

Because the triple-prime coordinate system represents the final body orientation, then

$$\begin{Bmatrix} X'''_B \\ Y'''_B \\ Z'''_B \end{Bmatrix} = \begin{Bmatrix} X_B \\ Y_B \\ Z_B \end{Bmatrix} \tag{32}$$

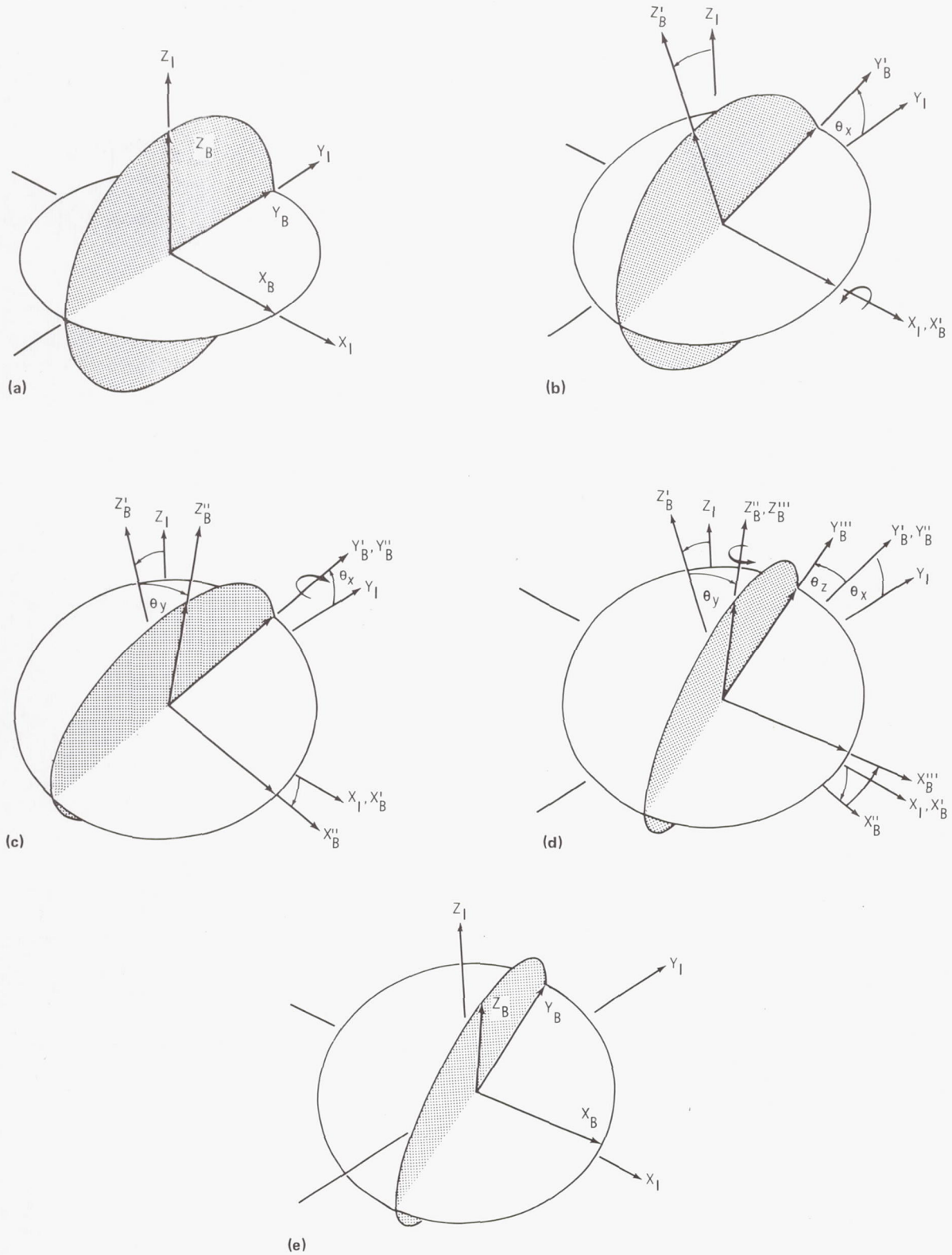

FIGURE 17.—Euler angle definition. (a) Body and inertial systems coinciding. (b) Rotation about X_B axis (θ_x). (c) Rotation about Y'_B axis (θ_y). (d) Rotation about Z''_B axis (θ_z). (e) Final orientation.

Combining matrix equations (29) through (32) gives

$$\begin{Bmatrix} X_I \\ Y_I \\ Z_I \end{Bmatrix} = \begin{bmatrix} T_{BI_{11}} & T_{BI_{12}} & T_{BI_{13}} \\ T_{BI_{21}} & T_{BI_{22}} & T_{BI_{23}} \\ T_{BI_{31}} & T_{BI_{32}} & T_{BI_{33}} \end{bmatrix} \begin{Bmatrix} X_B \\ Y_B \\ Z_B \end{Bmatrix} = [T_{BI}] \begin{Bmatrix} X_B \\ Y_B \\ Z_B \end{Bmatrix} \tag{33}$$

where
$$\begin{aligned} T_{BI_{11}} &= \cos\theta_y \cos\theta_z \\ T_{BI_{12}} &= -\cos\theta_y \sin\theta_z \\ T_{BI_{13}} &= \sin\theta_y \\ T_{BI_{21}} &= \sin\theta_x \sin\theta_y \cos\theta_z + \cos\theta_x \sin\theta_z \\ T_{BI_{22}} &= -\sin\theta_x \sin\theta_y \sin\theta_z + \cos\theta_x \cos\theta_z \\ T_{BI_{23}} &= -\sin\theta_x \cos\theta_y \\ T_{BI_{31}} &= -\cos\theta_x \sin\theta_y \cos\theta_z + \sin\theta_x \sin\theta_z \\ T_{BI_{32}} &= \cos\theta_x \sin\theta_y \sin\theta_z + \sin\theta_x \cos\theta_z \\ T_{BI_{33}} &= \cos\theta_x \cos\theta_y \end{aligned}$$

where $[T_{BI}]$ is the Euler transformation that transforms vectors expressed in the body system to vectors in the inertial system.

The Euler angle transformation $[T_{BI}]$ is orthogonal and thus its inverse is equal to its transpose.

$$[T_{BI}]^{-1} = [T_{BI}]^T \equiv [T_{IB}] \tag{34}$$

During a dynamic situation, the Euler angles are changing with time such that the integral of the Euler rate vector yields the Euler angles. The Euler rate vector is the projection of the body rate vector (ω_x, ω_y, ω_z) (expressed in the body coordinate system) on the nonorthogonal Euler rate axes system (X'_B, Y''_B, Z_B) or, mathematically,

$$\begin{aligned} [\omega_x(X_B) + \omega_y(Y_B) + \omega_z(Z_B) \\ = \dot{\theta}_x(X'_B) + \dot{\theta}_y(Y''_B) + \dot{\theta}_z(Z_B)] \end{aligned} \tag{35}$$

Matrix equations (30) and (31) yield

$$X'_B = \cos\theta_y (X''_B) + \sin\theta_y (Z''_B) \tag{36}$$

$$X''_B = \cos\theta_z (X_B) - \sin\theta_z (Y_B) \tag{37}$$

$$Y''_B = \sin\theta_z (X_B) + \cos\theta_z (Y_B) \tag{38}$$

$$Z''_B = Z_B \tag{39}$$

Substituting equations (36) through (39) into equation (35) gives

$$\begin{aligned} \omega_x(\hat{X}_B) + \omega_y(\hat{Y}_B) + \omega_z(\hat{Z}_B) \\ = (\dot{\theta}_x \cos\theta_y \cos\theta_z + \dot{\theta}_y \sin\theta_z)(\hat{X}_B) \\ + (\dot{\theta}_y \cos\theta_z - \dot{\theta}_x \sin\theta_z \cos\theta_y)(\hat{Y}_B) \\ + (\dot{\theta}_x \sin\theta_y + \dot{\theta}_z)(\hat{Z}_B) \end{aligned} \tag{40}$$

Putting equation (40) in matrix form

$$\begin{Bmatrix} \omega_x \\ \omega_y \\ \omega_z \end{Bmatrix} = [T_{EB}] \begin{Bmatrix} \dot{\theta}_x \\ \dot{\theta}_y \\ \dot{\theta}_z \end{Bmatrix}$$

$$= \begin{bmatrix} \cos\theta_y \cos\theta_z & \sin\theta_z & 0 \\ -\sin\theta_z \cos\theta_y & \cos\theta_z & 0 \\ \sin\theta_y & 0 & 1 \end{bmatrix} \begin{Bmatrix} \dot{\theta}_x \\ \dot{\theta}_y \\ \dot{\theta}_z \end{Bmatrix} \tag{41}$$

Solving matrix equation (41) for the Euler rate vector $(\dot{\theta}_x, \dot{\theta}_y, \dot{\theta}_z)$

$$\begin{Bmatrix} \dot{\theta}_x \\ \dot{\theta}_y \\ \dot{\theta}_z \end{Bmatrix} = [T_{EB}]^{-1} \begin{Bmatrix} \omega_x \\ \omega_y \\ \omega_z \end{Bmatrix}$$

$$= [T_{BE}] \begin{Bmatrix} \omega_x \\ \omega_y \\ \omega_z \end{Bmatrix}$$

$$= \frac{1}{\cos \theta_y} \begin{bmatrix} \cos \theta_z & -\sin \theta_z & 0 \\ \sin \theta_z & \cos \theta_z & 0 \\ -\sin \theta_y \cos \theta_z & \sin \theta_y \sin \theta_z & 1 \end{bmatrix} \begin{Bmatrix} \omega_x \\ \omega_y \\ \omega_z \end{Bmatrix} \tag{42}$$

where the matrix $[T_{BE}]$ is the inverse of $[T_{EB}]$.

The time derivative of equation (42) yields an expression for the time rate of change of the Euler rate components.

$$\begin{Bmatrix} \ddot{\theta}_x \\ \ddot{\theta}_y \\ \ddot{\theta}_z \end{Bmatrix} = [T_{BE}] \begin{Bmatrix} \dot{\omega}_x \\ \dot{\omega}_y \\ \dot{\omega}_z \end{Bmatrix} + \left(\frac{d}{dt} [T_{BE}] \right) \begin{Bmatrix} \omega_x \\ \omega_y \\ \omega_z \end{Bmatrix} \tag{43}$$

or

$$\ddot{\theta}_x = \frac{\left(\dot{\omega}_x \cos \theta_z - \dot{\omega}_y \sin \theta_z - 2\dot{\theta}_z \dot{\theta}_y + \dot{\theta}_y \omega_z \right)}{\cos \theta_y} \tag{44}$$

$$\ddot{\theta}_y = \dot{\omega}_x \sin \theta_z + \dot{\omega}_y \cos \theta_z + \dot{\theta}_x \dot{\theta}_z \cos \theta_y \tag{45}$$

$$\ddot{\theta}_z = -\ddot{\theta}_x \sin \theta_y - \dot{\theta}_y \dot{\theta}_x \cos \theta_y + \dot{\omega}_z \tag{46}$$

Differential equations (44) through (46) express the body angular rate and angular acceleration components in a form that can be conveniently integrated to yield the angular coordinates θ_x, θ_y, θ_z (the three Euler angles) that define the orientation of the rigid vehicle with respect to the inertial coordinate system. Many numerical integration schemes are available for solving equations (44) through (46). The numerical integration scheme used in the landing simulation was a variable step, with the time step set by the truncation error. This type of integration scheme worked satisfactorily for the Shuttle landing dynamics simulation.

1. Report No.	2. Government Accession No.	3. Recipient's Catalog No.
NASA RP-1056		

4. Title and Subtitle	5. Report Date
Orbiter Landing Loads Math Model Description and Correlation With ALT Flight Data	January 1980
	6. Performing Organization Code: JSC-16202
7. Author(s): David A. Hamilton, John A. Schliesing, and George A. Zupp, Jr.	8. Performing Organization Report No.: S-498
	10. Work Unit No.: 986-15-31-05-72
9. Performing Organization Name and Address: Lyndon B. Johnson Space Center, Houston, Texas 77058	11. Contract or Grant No.
	13. Type of Report and Period Covered: Reference Publication
12. Sponsoring Agency Name and Address: National Aeronautics and Space Administration, Washington, D.C. 20546	14. Sponsoring Agency Code

15. Supplementary Notes

16. Abstract

One objective of the Space Shuttle Approach and Landing Test (ALT) was to develop flight data for assessing landing gear characteristics and performance and for verifying landing dynamic analyses. The landing gears were instrumented with load-calibrated strain gages, a wheel-speed sensor, and strut stroke measurement devices. The mathematical procedure used in predicting the Shuttle touchdown loads and dynamics is presented together with the comparisons between measured flight data and the analytical predictions. Conclusions from these data are also presented.

17. Key Words (Suggested by Author(s))	18. Distribution Statement
Space Shuttle Orbiter Landing gear Aircraft tires Landing loads Spacecraft landing dynamics Impact loads Mathematical models Digital simulation	STAR Subject Categories: 15 (Launch Vehicles and Space Vehicles) 18 (Spacecraft Design, Testing, and Performance)

19. Security Classif. (of this report)	20. Security Classif. (of this page)	21. No. of Pages	22. Price*
Unclassified	Unclassified	27	$4.00

*For sale by the National Technical Information Service, Springfield, Virginia 22161

NASA-Langley, 1980